International Journal of Mechanical Sciences 231 (2022) 107580

Contents lists available at ScienceDirect

International Journal of Mechanical Sciences

journal homepage: www.elsevier.com/locate/ijmecsci

# Dynamic strength, reinforcing mechanism and damage of ceramic metal composites

Kuixin Lin [a], Meng Zeng [a], Hongmei Chen [a], Xiaoma Tao [a], Yifang Ouyang [a,*], Yong Du [b], Qing Peng [c]

[a] Guangxi Key Laboratory of Processing for Non-ferrous Metallic and Featured Materials, School of Physical Science and Technology, Guangxi University, Nanning 530004, China
[b] State Key Laboratory of Powder Metallurgy, Central South University, Changsha 410083, China
[c] State Key Laboratory of Nonlinear Mechanics, Institute of Mechanics, Chinese Academy of Sciences, Beijing 100190, China

ARTICLE INFO

*Keywords:*
Shock wave
Dislocation dynamic
Hugoniot elastic limit
Nanocomposites

ABSTRACT

Shock tolerance is desirable for ceramic particles-reinforced metal matrix composites in many applications, where the dislocation dynamics evolution under the extreme load is the key but still elusive. Herein, we have investigated the dislocation motion and interaction under shock loading of SiC/Al nanocomposites using molecular dynamics simulations. We have demonstrated that the plastic deformation occurs at an impact velocity (0.5 km/s) lower than the Hugoniot elastic limit of aluminum due to the reflected shear wave effect. The Al/SiC interfaces act as a dislocation emitter to control dislocation multiplication density and slip direction, opening a new pathway to achieve ultrahigh-strength via shock loading. When the impact velocity (1.0 or 1.5 km/s) exceeds the Hugoniot elastic limit, the effect of nanoparticles on dislocation structure has changed from multiplying to retarding dislocations. The spall strength of composites improves due to dislocations pile-up at interface. Instead, the damage in the matrix is exacerbated, owing to the enhanced residual peak stress and interface reflection waves. In addition, the effect of abnormal shock softening determined by atomic velocity is revealed, which could be suppressed by increasing impact energy dissipation. Meanwhile, dynamic compressive strength depends on pressure and dislocation structures evolution. Our atomistic insights might be helpful in designing advanced shock-tolerant materials.

## 1. Introduction

Ceramic particles-reinforced metal matrix (CPRMMs) composites (e.g. SiC, $Al_2O_3$ or diamond reinforced Al or Cu, etc. [1–4]) have been extensively exploited because of their unique physical and mechanical properties, including superior specific stiffness and strength, damage resistance, and high thermal conductivity [5–8], in addition to the relatively simple and numerous fabrication techniques compared with layered or fiber-reinforced composites [9–11]. Many experimental studies on CPRMMs observe high dislocation densities generation at the interface and ascribe it to the large mismatch of thermal expansion coefficients between metal (typically 20 ~30 $\times$ $10^{-6}K^{-1}$) and ceramic (typically 1~10 $\times$ $10^{-6}K^{-1}$), which is proposed to account for the unexpected high strength of these composite materials [12]. These CPRMMs composite materials contain a wealth of interfaces which altered drastically the mechanical behavior by controlling the dislocation dynamics evolution.

The effect of particle-size strengthening is one the most common and important mechanisms, which should be considered in the design and manufacture of CPRMMs. The yield strength of Al matrix composites with the SiC size of 10 μm is about 1.2 times of that of 50 μm one, due to the better load-bearing and the enhanced dislocation density [13]. Furthermore, studies show that when particle sizes decreased from microscale to nanoscale and low volume fractions (1~6 vol%) is used, Cu/SiC exhibits higher mechanical properties and electrical conductivity [14]. With decreasing size of nanoparticles, Orowan strengthening originating from the bowing force by dislocations bypassing the particles [15] and Hall-Petch effect coming from the resistance of grain boundary to dislocation slip [16] play dominant roles on the composite strength. The effect of Orowan strengthening reaches its peak at a critical particle size that is about 5.44 times the magnitude of the Burgers vector of dislocations [17]. The Orowan strengthening effect also

* Corresponding author.
*E-mail address:* ouyangyf@gxu.edu.cn (Y. Ouyang).

https://doi.org/10.1016/j.ijmecsci.2022.107580
Received 7 April 2022; Received in revised form 13 July 2022; Accepted 25 July 2022
Available online 28 July 2022

depends on the grain size in metal matrix that are usually polycrystals. When the crystal grains and nanoparticles were similar in size, most of the nanoparticles are distributed at grain boundaries (GB) [16]. As a result, the Orowan effect of nanoparticles mainly acts on the inside of grain, and it becomes weaker [18]. Meanwhile, the Hall-Petch effect enhances with increasing volume fraction of nanoparticles, because nanoparticles located at GB can effectively inhibit growth of crystal grain. In addition, the homogeneous distribution of SiC particles in composite lead to 4% enhancement in tensile strength [19]. Interestingly, the tensile strength of composite is about twice as matrix resulting from SiC particles gradient distribution [20], which means that laser shock-wave-driven nanoparticle implantation (LSWNI) [21] has great application prospect in composite manufacturing.

However, most of studies focus on analyzing the reinforcement mechanisms regarding the dislocation-nanoparticle and dislocation-grain boundary interactions during plastic deformation under quasi-static loading. Li et al. [18] proposed the dislocation bypassing particles prefers to occur when temperature increases, or particle size becomes smaller which reduce depinning stress. Zhang et al. [22] observed that the GB misorientation and strength have positive effect on mechanical responses of bicrystals, but no direct effect on the dislocation absorption and emission. Further, Bringa et al. [23] firstly studied shock strengthening effect for nano-crystalline copper. They found that the sliding barriers of GB and dislocation increase with shock pressure to achieve super-strength. It is noticeable that the relationship between interaction dislocations and microstructure with correlated mechanical response is gradually recognized. The interaction and evolution of the dislocations include their multiplication, intersection, reaction, annihilation, which are expected to play roles in shock strengthening. However, limited data and reports are available in the literature. Consequently, it is still elusive about the reinforcement mechanism under shock loading and the effect of ceramic-metal interface as dislocation source on the strength of the CPRMMs.

Shock loading means mechanical loading with extreme strain rate. Under shock loading, the deformation of material is a very complex dynamic procedure, resulting in significant changes in the physical-mechanical properties of composites. The shock-waves are generated within the composite. The shockwaves then transmit and reflect on the interface [24–27]. Studying the structural dynamic evolution and damage mechanisms of the composites is experimentally challenging. The experimental and theoretical studies to understand the dynamic behaviors of CPRMMs under shock loading are infrequent and incomplete. The previous studies simply focus on the influence of morphology of particles, strength of matrix-reinforcement bonding, and process combinations for the shock response of CPRMMs [28–31]. The underlying micromechanisms are still unsettled.

It is desirable to explored the micromechanisms of shock strengthening for material design of CPRMMs and process optimization of laser shock peening (LSP). It is reported that the improved fatigue life and mechanical properties after LSP are due to the formation of LSP-induced compressive residual stress (CRS) and grain refinement (GR) at the materials surface layer [32–34]. Some studies suggest that both CRS and GR depend on the dislocation slip and multiplication [35–37]. It is worth mentioning that these studies are on alloys, where only the effect of the interaction between the grain boundary and shock wave on the induced dislocation structure is considered. For composites, Cui et al. [38] discovered that the SiC nanoparticles were embedded into the pure Al surface structure by LSWNI, which achieves highly stable and ultra-high CRS. However, the LSP-induced residual stress of SiC/2009Al composites is relaxed to 50% when subjected to thermal loading (100 °C for 50 h) [39]. Thus, the key factors determining the properties of LSP-induced residual stress in composites are still unknown. The increasing in content of the reinforcement, (TiB+TiC)/Ti-6Al-4 V composite results in higher dislocation density in the matrix and the formation of GR near the interface by shot peening [40]. Therefore, it is of great significance to study how the microstructure and dislocation dynamically evolves during the application of LSP on composites. It is crucial to identify the key factors such as interface and strain rate.

In the past decades, molecular dynamics (MD) simulation has been established method for investigating the dislocations. It is widely used to study the shock loading deformations of various composites involved ceramic-metal nanolayered, carbon nanotubes or graphene-metal etc. [41–44]. Al/SiC nanocomposite is one of the common CPRMMs, and therefore chosen as a model material for this study. we have used MD simulation to analysis the shock wave profile and dislocation dynamics evolution to reveal the elastic-plastic mechanical responses of CPRMMs under shock loadings. The work focuses on shape effects of the reinforcement on shock responses of composite, according to particle shape has a close influence on stress intensity and distribution in materials [45, 46].

## 2. Methods and model

To understand the effect of reinforcement, we initially construct two models, with and without nanoparticles, respectively, for comparison. The former model is a monocrystalline Al (M-Al) with $40\times20\times100$ nm$^3$ orientated along the $x$-[100], $y$-[010] and $z$-[001] crystallographic directions (~5 million atoms), as shown in Fig. 1(a). The periodic boundary condition (PBC) is applied in the $x$- and $y$-directions. The free boundary conditions (FBC) is used along the z-direction for the shock loading. The latter model includes three spherical-SiC or cubic-SiC nanoparticles as reinforcements with a volume fraction of 1.3% added to Al matrix (Fig. 1(b)). The model embeds completely SiC nanoparticles into Al-matrix to make nanoparticles are free and no periodic boundaries. The interfaces are relaxed according to the energy minimization later during equilibration process.

The non-equilibrium molecular dynamics (NEMD) simulations were carried out using the classical MD employed in LAMMPS program [47] to investigate the influences of dislocation dynamics evolution under shock loading on plasticity and stress responses in Al/SiC nanocomposite. The embedded atom method (EAM) inter-atomic potential developed by Winey et al. [48] is used for Al, which describes accurately the stacking-fault energy and has been adopted for simulating shock behaviors of M-Al under impact loading [49,50]. Because the modulus of SiC-reinforcements is quite distinct from that of Al-matrix, the deformation of SiC is minor at shock process. Thus, the Tersoff potential [51] is adopted to reproduce the mechanical response of SiC without phase transformation in this work. Besides, for the interface interactions between SiC and Al, a Morse pair-wise potential is used [52]. This potential is obtained in curve fitting to ab initio data, and verified in other studies [53].

Before dynamic calculation, the systems have been initially relaxed via energy minimized using the conjugate gradient method. The criterion of energy convergence is $1.0\times10^{-4}$eV for the whole system (about $10^{-11}$eV/atom). Then the models have been further relaxed in isothermal-isobaric (NPT) ensemble with temperature $T = 300$ K and zero pressure for 50 ps to reach equilibrium. During the relaxation, the periodic boundary conditions were applied to all the three directions. Finally, the shock simulations have been carried out in the micro-canonical (NVE) ensembles with a timestep of 0.0005 ps.

The shock loading is simulated by a virtual infinite-mass piston at left end of the model. The piston has a constant impact velocity ($U_I$) (=0.5, 1.0, or 1.5 km/s) to produce stable shock waves. The velocity of atoms in loading area is denoted as $U_p$ (particle velocity). The velocity of atoms at interface between loading and unloading area is expressed as $U_s$ (wave velocity). The values of $U_I$ are chosen because with which the loading stress is lower or higher than the Hugoniot elastic limit (HEL) of Al (~12 GPa for hydrostatic pressure).

Shock wave propagation characteristics along the $z$-direction are described using 1D binning analysis, with a bin width of 1.25 nm [54]. The simulation domain is divided into 40 bins with equal size. Critical mean physical properties including the hydrostatic pressure ($p$),

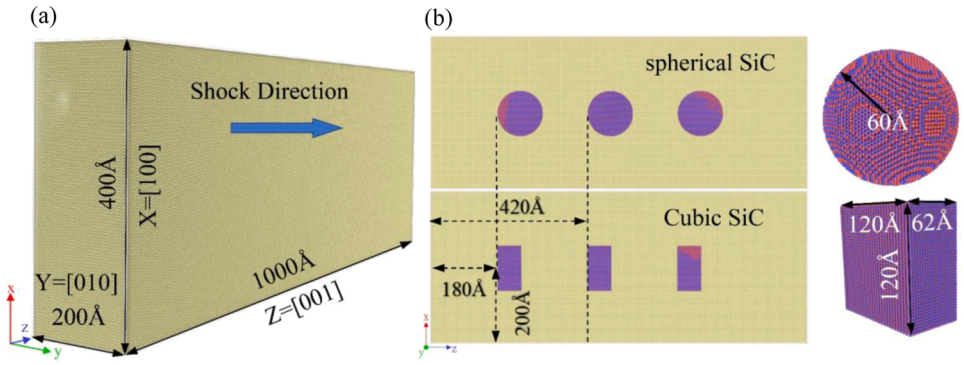


**Fig. 1.** (a) A three-dimensional model of M-Al; (b) Geometrical characteristics of the spherical-SiC/Al and Cubic-SiC/Al nanocomposites. The incident shock wave is along the positive z direction [001].

maximum shear stress ($\tau$), von mises stress ($\sigma_{VM}$), and temperature of the shocked systems were determined respectively from the following equations:

$$p = -\frac{1}{3}(\sigma_{xx} + \sigma_{yy} + \sigma_{zz}) \tag{1}$$

$$\tau = \frac{1}{2}\left[\sigma_{zz} - \frac{1}{2}(\sigma_{xx} + \sigma_{yy})\right] \tag{2}$$

$$\sigma_{VM}^2 = \frac{1}{2}\left[(\sigma_{xx} - \sigma_{yy})^2 + (\sigma_{yy} - \sigma_{zz})^2 + (\sigma_{zz} - \sigma_{xx})^2\right] \tag{3}$$

and

$$T = \frac{2}{3N_a}\sum_{1}^{N_a}\frac{E}{k_B} \tag{4}$$

where $\sigma$ represents the principal stress for three components of tensor, $N_a$ is the total number of atoms in specified group, $E$ is the kinetic energy of each atom, and $k_B$ is the Boltzmann constant. The visualization and analysis are achieved using OVITO [55]. We have employed the common neighbor analysis (CNA) [56] to identify the crystal structure, and dislocation extraction algorithm (DXA) [57] to determine the Burgers vectors of the dislocations. The total length of the dislocation lines as $L_t$ and the volume of the current configuration as $V_c$ are obtained by the DXA. The dislocation density ($D_d$) was calculated based on formula of $D_d = L_t/V_c$, to evaluate plastic deformation of the sample.

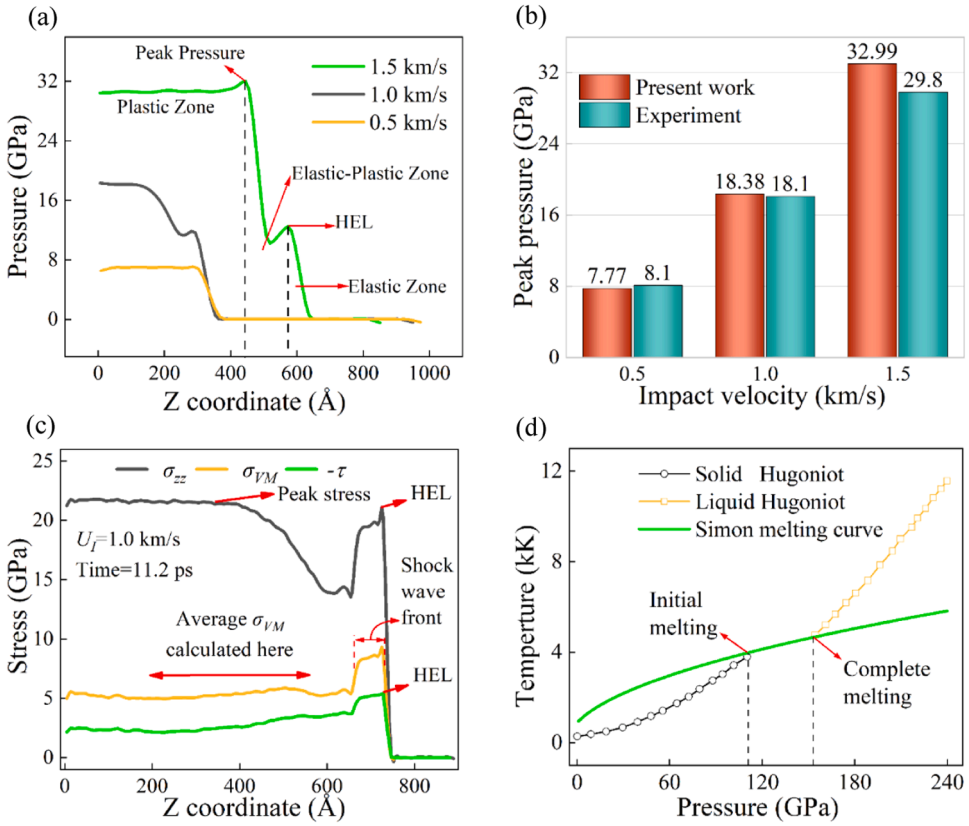


**Fig. 2.** The shock wave propagation in M-Al at three impact velocities: 0.5 km/s, 1.0 km/s, and 1.5 km/s. (a) Pressure profiles predicted by the NEMD; (b) Comparisons of the peak stress between present simulations and experimental measurement [58]. (c) The wave stress profiles of $\sigma_{zz}$ and $\tau$ for M-Al with the HEL = 21 GPa and 5.2 GPa, respectively, and von mises stress at $U_I$ = 1.0 km/s. (d) The Simon melting cure, solid and liquid Hugoniots of M-Al.

## 3. Results and discussion

### 3.1. Shock hugoniot in M-Al

We have firstly investigated the effect of magnitude of shock-wave peak stress (or pressure) on the plasticity and shock responses in M-Al under shock loading to ensure the accuracy of model and method. Fig. 2 (a) and (b) present the pressure profiles of M-Al at different impact velocities from NEMD simulations comparing with experimental measurements. For impact velocity $U_I = 0.5$ km/s, there is only elastic waves and no plastic deformation. The shock wave profile is divided into three deformation zones at $U_I = 1.0$ and 1.5 km/s: a zone of elastic front wave with rapidly increasing stress, a zone of elastic-plastic with initial plastic transformation, and a zone of plastic with stable flow stress. Compared to the experimental measurement, the relative error of calculated peak pressure is within 5% for $U_I = 1.0$ km/s and 10% for $U_I = 1.5$ km/s. The consistency between the simulation and the experimental measurements indicates that the EAM potential and the structural model are appropriate. Fig. 2(c) provides the HEL of M-Al impacted at $U_I = 1.0$ km/s for maximum shear and principal stress as a criterion for its plastic deformation. When $\sigma_{zz}$ increases, $\tau$ increases until the onset of plasticity occurs. The flow stress is identified with average $\sigma_{VM}$ far behind the shock wave front, which is an indirect method to determine dynamic compressive strength [23]. In Fig. 2(d), shock melting pressure is 111 GPa calculated from Simon melting equation [59] along with the principle Hugoniot [60]. Because the peak pressures (Fig. 2b) are much less than the shock melting pressure, the aluminum maintains its crystal structure in the three examined systems. Therefore, dislocation and crystal orientation theories are still availability.

### 3.2. The interaction of interface with shock-wave

The shock wave penetrates and propagates in the composites, where it may create some new microstructures. These shockwave-induced microstructures affect the properties of composites in turn. We firstly study a simple case of which only the elastic wave is considered. When the initial impact velocity $U_I = 0.5$ km/s, the maximum shear stress (MSS) is displayed in Fig. 3(a) for the three models subjected to shock loading at ambient temperature. The MSS of M-Al stabilized at about 3.0 GPa behind the shock wave front, implying non-plastic deformation in the system. Here, the decline in the MSS of M-Al after the peak results from $U_S > U_P$ leading to compression deformation relaxation. However, the MSS of cubic-SiC/Al(C-SiC/Al) and spherical-SiC/Al (S-SiC/Al) nanocomposites drops to a lower level (1.3 GPa). The reason is that the lattice slipping is activated and the obstacle in the models is too slight to block dislocation motion to released stress.

As the simulation proceeds, the density of dislocations grows significantly when the shock wave arrived at the SiC/Al interface at 3 ps, as shown in Fig. 3(b). The dislocations formed by extracting or inserting one-layer atom from the face centered cubic (FCC) lattice create stacking faults (red segment), and the nucleation of dislocation only generates on some specific area of defective surface (blue segment). Besides, for an 0.5 km/s shock loading, the nanocomposites exhibit substantial dislocations, as presented in Fig. 3(c) and (d) for cubic- and spherical-SiC/Al system, respectively, while M-Al is completely absent of dislocations.

As aforementioned, plastic deformation occurs easier in nanocomposites due to the existence of SiC nanoparticles. When the shock wave front reaches the surface of SiC nanoparticles at $t = 3.25$ ps, favorable nucleation sites (FNS) of dislocations are observed. FNSs are located on the edges of lateral-surface of cubic-SiC, and two circle belts on the surface of spherical-SiC, as illustrated in Fig. 4. (a) and (b), respectively. It is crucial to investigate the mechanisms of the reinforced SiC inducing dislocation nucleation, and the induction mechanisms may depend on the geometrical shape of SiC. In the C-SiC/Al, shock waves propagation through the interface is from a medium incident vertically to another medium with different acoustic resistance. From continuous wave theory and Newton's third law [61], the interactions between incident compression wave (irrotational wave) and interface would result in the transmission and reflection of stress wave, and both the propagation directions of the produced waves are still parallel with the incident wave. Owing to the normal components of $\sigma_{zz}$ in the direction of shock loading, it is crucial for determining the stress state of systems.

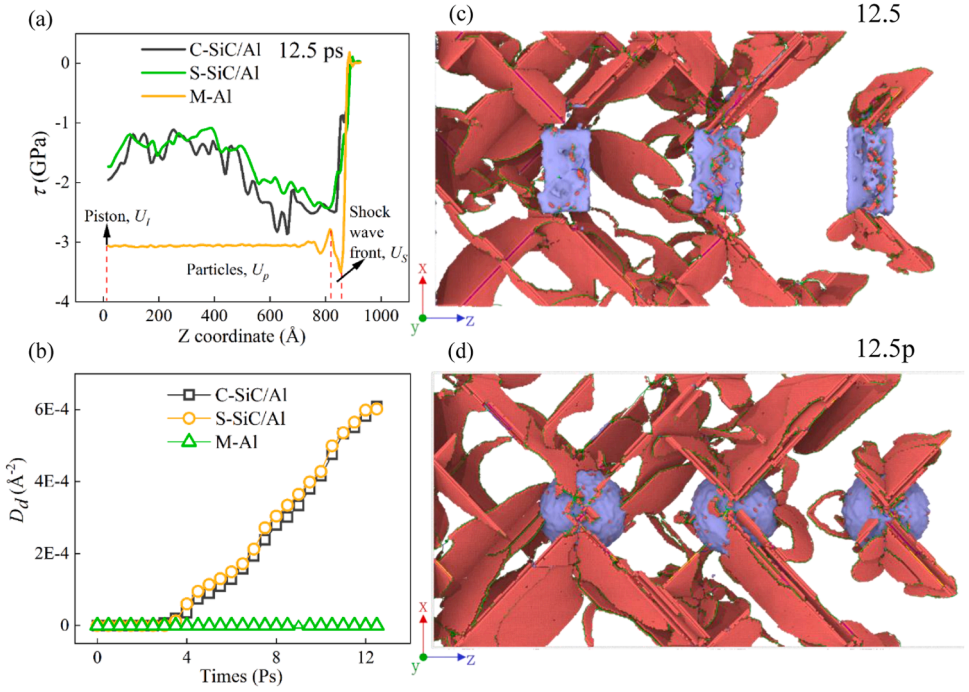


**Fig. 3.** (a) The maximum shear stress $\tau$ profiles of the nanocomposites at 12.5 ps after piston started to move with $U_I = 0.5$ km/s. The particles have a velocity $U_P = U_I$, behind the shock wave front (giving $U_S \approx 0.7$ km/s). (b) The dislocation densities $D_d$ as a function of time. (c) The lattice slipped at 12.5 ps in cubic-SiC/Al, compared to (d) sphere-SiC/Al. Red (blue) part denotes stacking fault (defect surface).

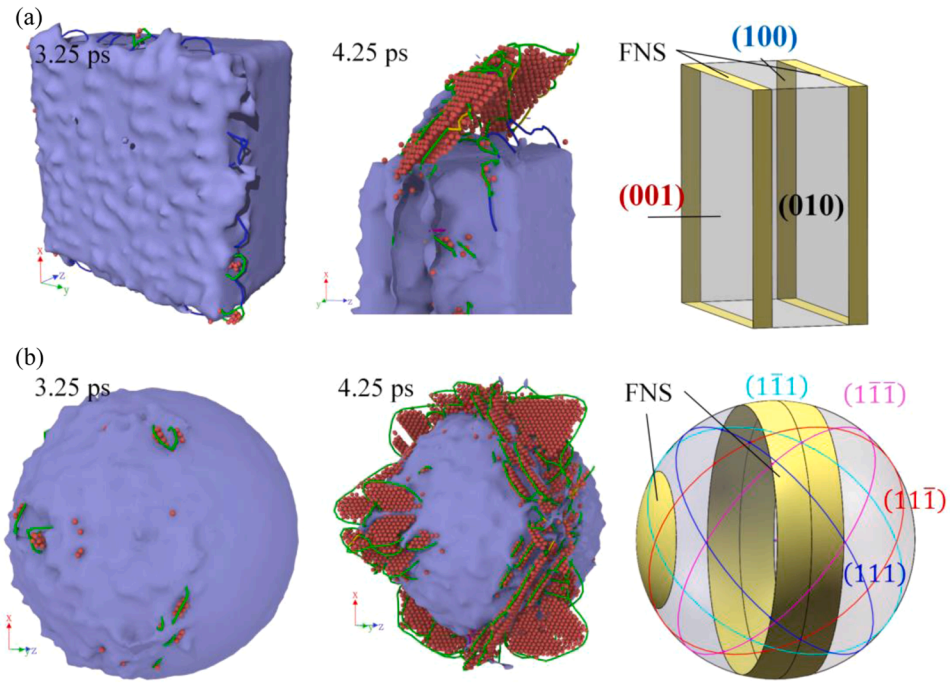


**Fig. 4.** Surface dislocation nucleation in two nanocomposites of (a) C-SiC/Al; (b) S-SiC/Al under 0.5 km/s at the times range: 3.25–4.25 ps. The green lines are Shockley partial dislocations, and the navy-blue lines are perfect edge dislocations in figures. The rightmost simplified 3D view in figures illustrate the favorable nucleation sites (FNS) on the surface of the corresponding SiC nanoparticles with cubic (top) and sphere (bottom) geometry. (For interpretation of the references to color in this figure legend, the reader is referred to the web version of this article.)

In metals, pure tension or compression loading needs sufficient resolved shear stress ($\tau_r$) and suitable slip systems to accommodate the plastic deformations. The relationship between the compression stress $\sigma_{zz}$ and resolved shear stress is expressed as

$$\tau_r = \sigma_{zz}\cos\lambda\cos\varphi = m\sigma_{zz} \tag{5}$$

where $\lambda$ ($\varphi$) denotes the angle between the stress axis and the normal to the slip plane (the slip direction) for a slip systems of FCC crystal, $m$ is a well-known Schmid factor. Therefore, the directions of above three stress waves directly related to the $\sigma_{zz}$ is discussed.

According to the momentum conservation of the shock wave fronts, and the condition that the stresses of particle on both sides of the interface are identical, we obtain the following relationships:

$$n = (\rho_0 C_0)_1/(\rho_0 C_0)_2 \tag{6}$$

$$\sigma_R = \frac{1-n}{1+n}\sigma_I = F\sigma_I \tag{7}$$

$$\sigma_T = \frac{2}{1+n}\sigma_I = T\sigma_I \tag{8}$$

where subscripts *I*, *R*, and *T* represent the stress associated respectively with the wave of incident, reflection, and transmission; $n$ is the ratio of acoustic impedance of the medium; $\rho_0$ is the intrinsic density of material; $C_0$ is the elastic wave velocity; the subscripts 1 and 2 denote two media; $F$ and $T$ are called the reflection and transmission coefficient.

In present study, the acoustic impedance of Al and SiC are $(\rho_0 C_0)_1 = 18 \times 10^5 \mathrm{g/cm^2 \cdot s}$ and $(\rho_0 C_0)_2 = 48 \times 10^5 \mathrm{g/cm^2 \cdot s}$, respectively. When the stress wave propagates cross an interface 1 from Al to SiC, the values of $n\langle 1, F\rangle 0$, and $T > 1$ denote the mismatch in the acoustic impedance of the adjacent layers. This causes the reflected wave stress loading. The stress amplitude of the transmitted wave is larger than that of incident waves, resulting in increase of wave-front stress in the $\sigma_{zz}$. From Fig. 5 (a), when shock wave arrives the interface 1, the maximum value of $\sigma_{zz}$ = 14 GPa at 3.0 ps is lower than the $\sigma_{HEL}$ of M-Al = 20 GPa (from Fig. 2 (c)). When shock wave passes through interface 2 from SiC to Al, transmitted wave stress is decreasing. The simulation results accord with

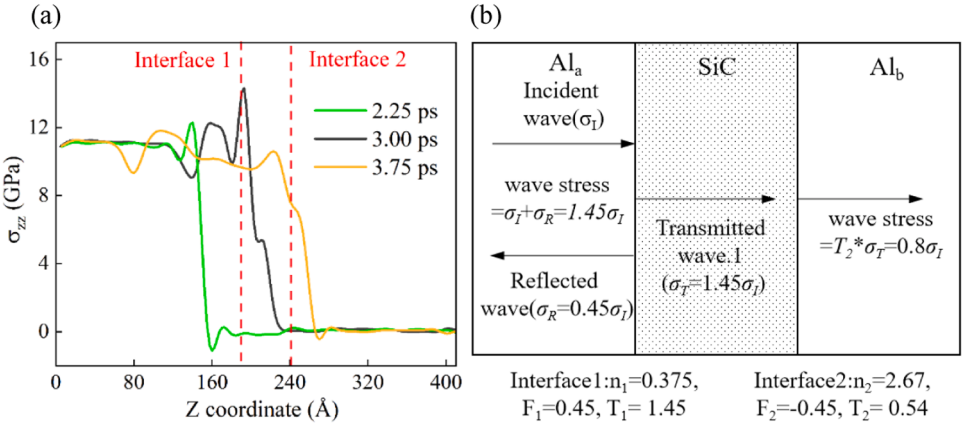


**Fig. 5.** (a) The principal stress $\sigma_{zz}$ distribution for the C-SiC/Al with $U_I = 0.5$ km/s at time instants of 2.25, 3.00 and 3.75 ps; (b) Schematic diagram of shock wave propagation dynamics process in the C-SiC/Al.

results of calculation in Fig. 5(b). Therefore, no plastic deformation occurs in Al crystal nearing interfaces perpendicular to impact direction.

For the S-SiC/Al, the shock compression wave ($P_I$) is oblique incidence on the curved surface of spherical-SiC, leading to the coupled reflection of both the irrotational wave ($P_R$) and the shear wave ($S_R$) also as equivoluminal wave, as illustrated Fig. 6(a). The surface of reflection resembles to the tangent plane of reflection point on the spherical surface. The incident angle between the $P_I$ direction and the normal to the reflective plane ($N_L$) represented by $\alpha_I$, and the reflected angles between the $P_R$ ($S_R$) direction and the $N_L$ represented by $\alpha_R$ ($\beta_R$).

The introduction of the latitude and longitude coordinate system for convenience, the latitude angle of reflection point is denoted as $\alpha_L$, with $\alpha_I + \alpha_L = 90^\circ$. The direction of the reflected wave varies with $\alpha_L$ as displayed in Fig. 6(b). The reflection coefficients of the $P_R$ and $S_R$ wave are calculated by the following equations:

$$\delta_{P_R} = \frac{\sin(2\alpha_I)\sin(2\beta_R) - k^2 cos^2(2\beta_R)}{\sin(2\alpha_I)\sin(2\beta_R) + k^2 cos^2(2\beta_R)}, \tag{9}$$

$$\delta_{S_R} = \frac{2k\sin(2\alpha_I)\sin(2\beta_R)}{\sin(2\alpha_I)\sin(2\beta_R) + k^2 cos^2(2\beta_R)}. \tag{10}$$

The reflection coefficients are a function of Poisson's ratio and the incident angle are obtained from Eqs. (9) and (10). The $k = \sqrt{\frac{2(1-\nu)}{1-2\nu}}$, $\nu$ is Poisson ratio for aluminum.

The simulated shock stress response of nanocomposites initially orients along the [001] axis. When stress wave is reflected from the spherical surface, the occurrence of stress axis rotation leads to Schmid factor to change correspondingly. Fig. 6(c) shows the Schmid factor varies with reflected angle for three slip systems whose slip plane is (111). For simplification, reflected angle is restricted to the (101) plane. The compressive stress of $P_R$ relies on its resolved shear stress to produce plastic deformation ($P_I = 11$ GPa at $U_I = 0.5$ km/s). Thus, the resolved shear stress of $P_R$ could be calculated by the Eq. (5), combining the data of Schmid factor and reflection coefficient in Fig. 6(c) and (d). The slip systems of (111) [01–1] and (111) [−101] become more inclined to be inactivated as the resolved shear stress on them decreases in Fig. 6(e). Although the resolved shear stress shows a general increasing trend on the (111) [1–10], they are still less than 5.2 GPa. These results confirm that the reflected irrotational wave $P_R$ is not an origin for shear strain.

Unlike the case of irrotational wave, a shear wave is created when the atoms in the lattice are moving perpendicular to the wave direction, inducing shear stress in the material when the waves propagate through. The condition of plastic deformation in the FCC crystal is that the component of shear stress ($\tau_C$) on the slip direction of 12 slip systems over critical shear stress (CSS) = 5.2 GPa. Fig. 6(f) shows that the component of shear stress on the (111) [1–10] system exceeded the CSS within a band of low latitude angle ($0^o < \alpha_L < 50^o$), consistent with MD results of the latitude angle of favorable dislocations nucleation sites (shown in Fig. 4(b)). These results demonstrate that the reflected shear waves are the source of driving force for dislocations activities (nucleation, multiplication, and reaction), triggering plastic strain relaxation. Inspired by this discovery, we infer that incident wave decomposes to reflected shear waves on the edges of cubical-SiC. It is also the main reason of shock-induced plastic deformation. Meanwhile, this offers a novel explanation about the formation of high-density dislocations around nanoparticles in composites after mechanical processing or heat treatment.

### 3.3. Dislocations dynamic evolution

The dislocations generated by shock wave have been reported in displacement cascades during irradiation damage [62]. The shock response of materials is determined by the interaction and evolution of

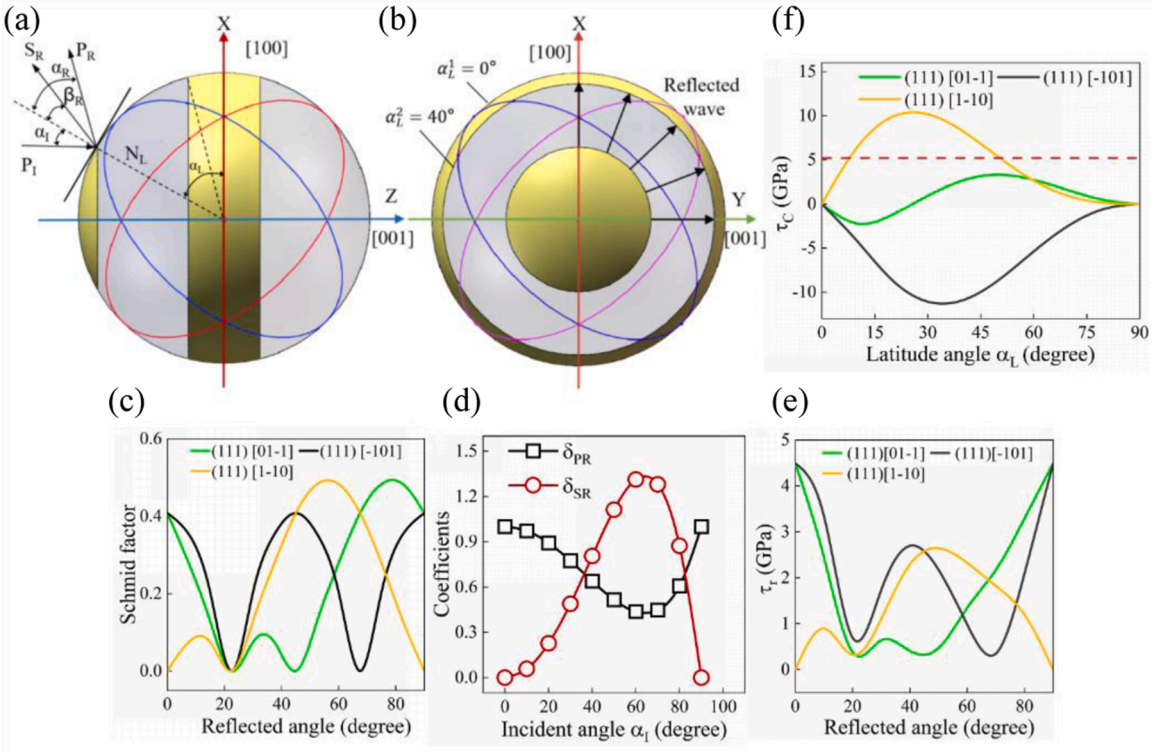


**Fig. 6.** Stress wave reflection schematic illustrations of spherical surface. (a) $P_I$ is the incident compression wave; $P_R$ and $S_R$ are reflected irrotational and shear wave; $\alpha_I$, $\alpha_R$, and $\beta_R$ are the angles between three waves and normal $N_L$, respectively; $\alpha_L$ is the latitude angle. (b) The random arrows denote the distribution of reflected waves on the spherical-SiC. (c) The Schmid factors of $P_R$ for three slip systems as a function of the reflected angles. (d) Reflected coefficients of $P_R$ and $S_R$ versus incident angles curves. (e) The resolved shear stress of $P_R$ as a function of the reflected angle. (f) The component of shear stress ($S_R$) in the slip crystal orientation as a function of the latitude angle of reflection point.

the defects, such as dislocations, stacking faults, and voids. Since dislocations play a vital role in crystals plasticity and dynamic response, the dislocations dynamics process should be deeply delved. Under the shock loading, the existing dislocations multiplication and slipping are not enough to release large shear stress, which lead to the dislocation homogeneous nucleation [63], as illustrated in Fig. 7. The dislocation lines are colored by their Burgers vector. The evolution of dislocation structure dates from the perfect dislocation, which will dissociate into two energy-dominant partial dislocations. Then they develop into some small loops shown in Fig. 7(a) and (b). As these coupled loops grow larger, Shockley partial dislocations intersected to provide internal pinning points as seen from Fig. 7(c), to initiate the double cross-slip multiplication mechanism as shown in Fig. 7(d). This is more efficient than Frank-Read dislocation source. Consequently, even if the nucleation sites in C-SiC/Al are less than those of S-SiC/Al, the dislocation density of C-SiC/Al increases almost as rapid as the S-SiC/Al. The dislocation forest is formed if the self-multiplication mechanism has generated a high enough dislocation density as illustrated in Fig. 7(e). On the main slip systems of S-SiC/Al, the slip direction of the dislocations is splayed, as shown in Fig. 7(f), resulting in that the dislocations almost do not intersect.

Since the dislocations are emitted from the interface of Al/SiC, the interaction between crystal defects is the main factor affecting the mechanical response of the composites. In the C-SiC/Al, when Shockley dislocation $\frac{1}{6}[\bar{1}12]$ (p1) contacts the stacking fault (SF) of slip system $\frac{1}{6}[1\bar{1}2](1\bar{1}\bar{1})$, the width of SF is greater than the length of dislocation p1 so that dislocations cannot bypass obstacles, resulting in that the dislocations have to form very narrow angles around the obstacles to bypass them [11], as shown in Fig. 8(a).

Interestingly, the dislocation p1 starts to transform to an immobile stair-rod dislocation $\frac{1}{6}[10\bar{1}]$ (SR), even the already passed section of dislocation p1 is pulled back, as shown in Fig. 8(b) and (c). Subsequently, the next Shockley dislocation (p2) moves and is captured by SR to form an only climbing Frank dislocation $\frac{1}{3}[1\bar{1}\bar{1}]$, shown in Fig. 8(d). In addition, the reaction between extended dislocations provokes an immobile Hirth dislocation $\frac{1}{3}[0\bar{1}0]$. The annihilation between the two dislocations with opposite motion, acting as the obstacles of dislocation movement, are observed in the evolution of dislocation, as shown in Fig. 8(e) and (f). The obstacles exist in the main slip directions of slip system $\frac{1}{6}[1\bar{1}2](1\bar{1}\bar{1})$. Therefore, the dislocations on the primary slip plane are surrounded by the dislocations on the secondary slip plane to

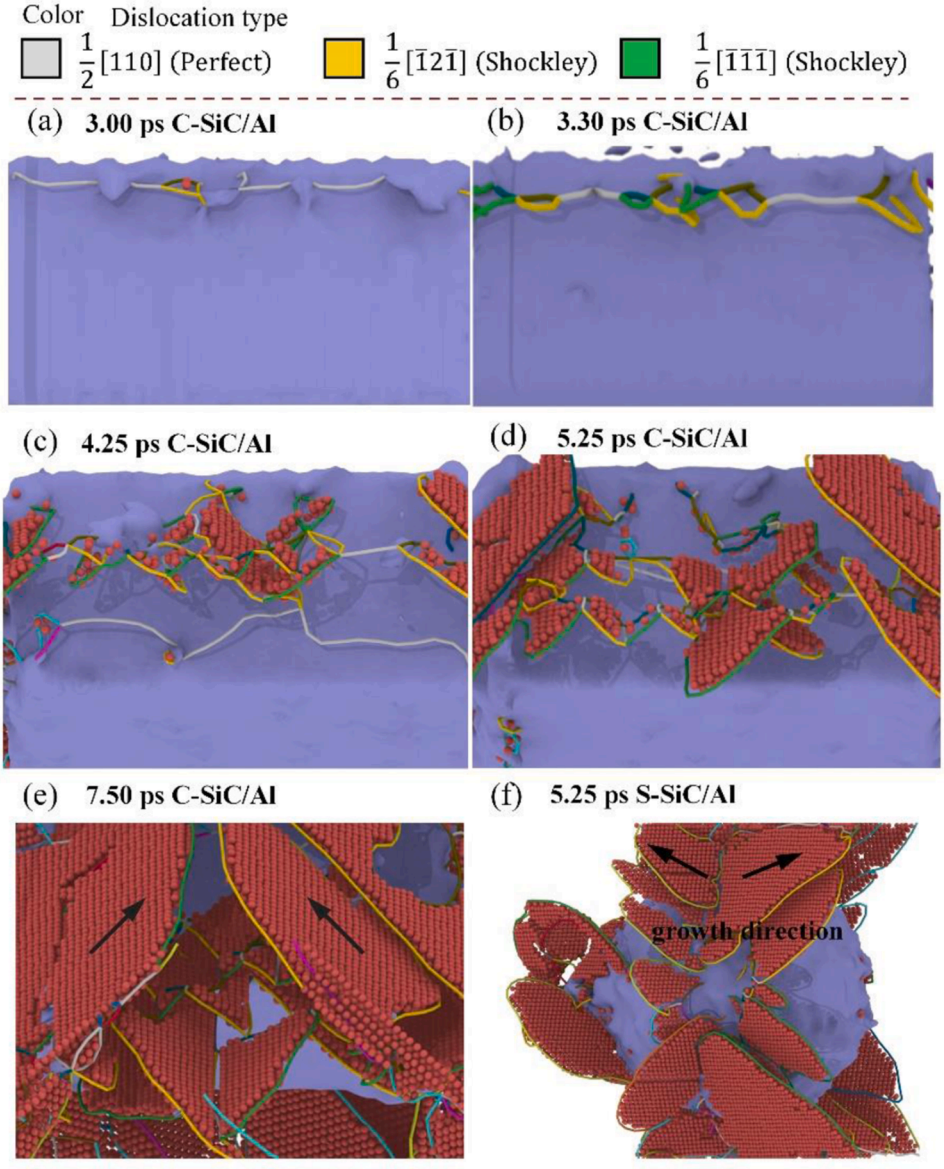


**Fig. 7.** The dislocation multiplication processes in the nanocomposites. (a) 3.00 ps in C-SiC/Al; (b) 3.30 ps in C-SiC/Al; (c) 4.25 ps in C-SiC/Al; (d) 5.25 ps in C-SiC/Al; (e) 7.50 ps in C-SiC/Al; (f) 5.25 ps in S-SiC/Al. The dislocations lines are colored by Burgers vector (except as marked in the figures, all others are partial dislocations). The arrow indicates the direction of dislocation slip. (For interpretation of the references to color in this figure legend, the reader is referred to the web version of this article.)

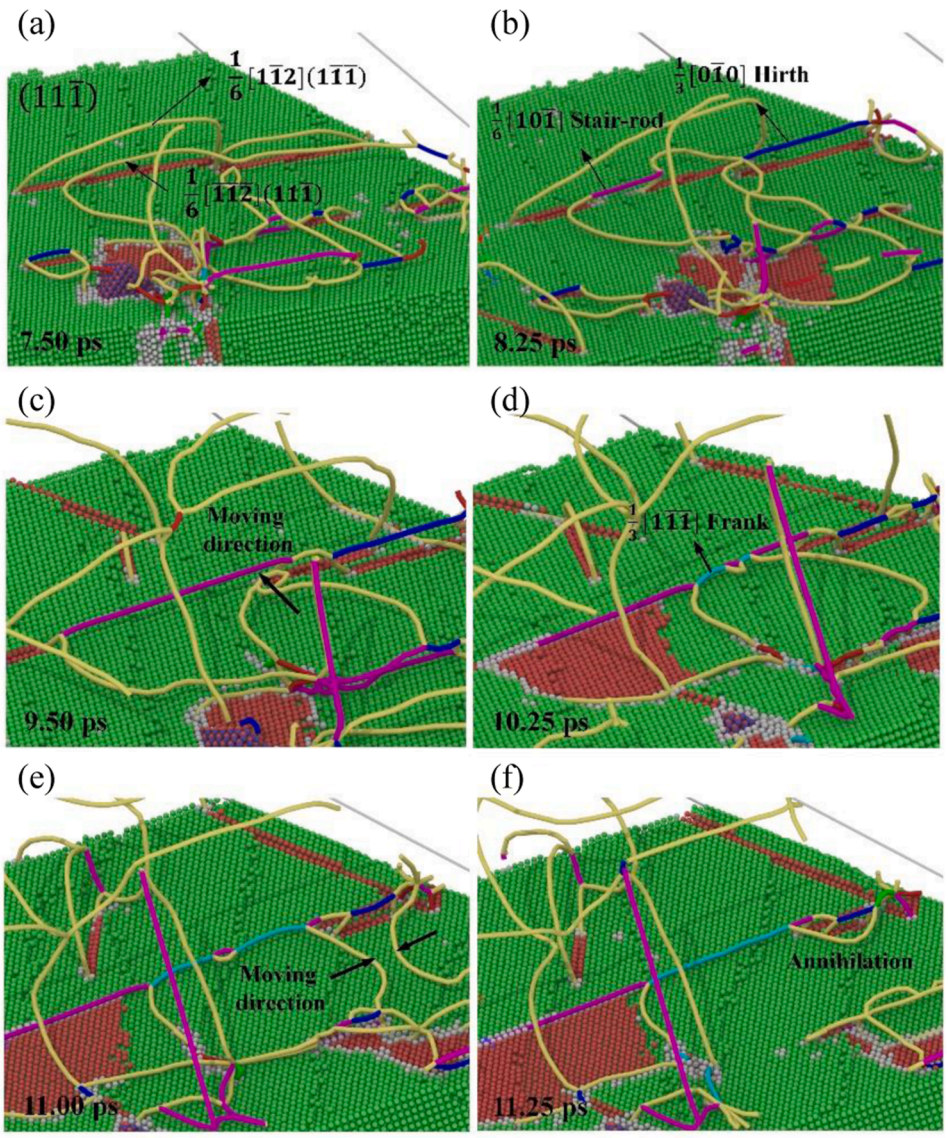


**Fig. 8.** Interaction of dislocation with the stacking fault (or dislocation) in the C-SiC/Al from section view of $(11\bar{1})$ plane (the dislocations lines are colored by dislocation type): (a) 7.50 ps; (b) 8.25 ps; (c) 9.50 ps; (d) 10.25 ps; (e) 11.00 ps; (f) 11.25 ps. The Shockley, Frank, Stair-rod, and Hirth dislocations are represented in yellow, sky-blue, purple, and dark-blue lines, respectively. (For interpretation of the references to color in this figure legend, the reader is referred to the web version of this article.)

be stored in crystal. The interaction of defects increases the shear stress required for the deformation in the C-SiC/Al.

Nevertheless, Fig. 9 clearly shows that the dislocations slip obstructions are less in the S-SiC/Al than that in C-SiC/Al, evidencing with the larger shear stress drop (Fig. 3(a)). Especially, the dislocation motion is weakly affected by immobile Hirth dislocation that is relatively unstable. With the impacts from Shockley dislocations, the Hirth dislocation disassociates more easily than the stair-rod dislocation, as shown in Fig. 9, which is verified by the energy barrier of $E_S = 0.6$ eV for the stair-rod lock overtops that of $E_H = 0.2$ eV for the Hirth lock [64].

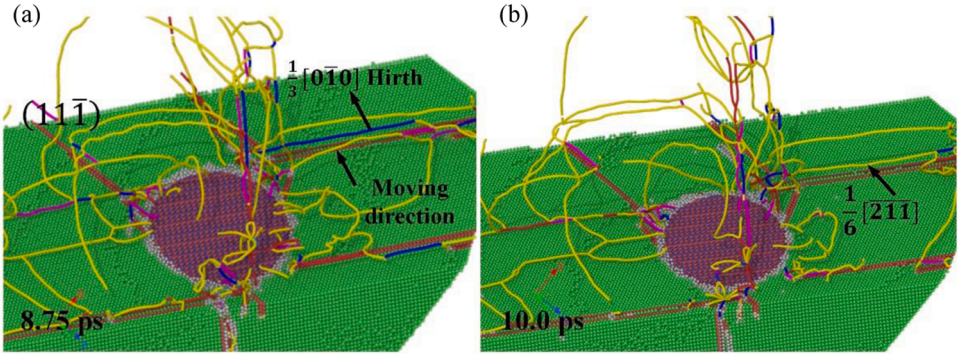


**Fig. 9.** Dislocations microstructure in the S-SiC/Al at (a) 8.75 ps and (b) 10.0 ps. The lines depict dislocations. The Shockley, Frank, Stair-rod, and Hirth dislocations are represented in yellow, sky-blue, purple, and dark-blue lines, respectively. (For interpretation of the references to color in this figure legend, the reader is referred to the web version of this article.)

To differentiate the contribution of immobile dislocations, the total length of two immobile dislocation obtained for the C-SiC nanocomposite is compared to that of the S-SiC/Al nanocomposite, as shown in Fig. 10(a). The length of stair-rod dislocation has all along maintained a faster growth throughout the simulation process of C-SiC/Al than the S-SiC/Al, signifying that the dislocations have not reached saturation to continue absorbing impact energy. However, total length of Hirth dislocations reaches a constant value after 10 ps in the C-SiC/Al, while that in the S-SiC/Al appears to decrease after 11.5 ps. Both behaviors support the weak nature of Hirth dislocation. Overall, the results suggest that the C-SiC/Al yields higher material strength (or stiffness) and toughness during the shock compression at $U_{\mathrm{I}} = 0.5$ km/s. The strength is the ability of a materials to resist plastic deformation, whereas the toughness refers to the ability of a materials to absorb energy during plastic deformation [65].

### 3.4. The spall fracture and dynamic compression

The spallation is a common damage process determined by the weakest links in structure during shock loading. With the stress wave propagating in the structure, the two rarefaction waves in opposite directions superpose and interact to generate a dynamic tension area. Once the tension stress over the cohesion of crystal (spall strength), the voids start to nucleate, grow, and accumulate. Then they lead to materials spall failure. The experimental evidences [66–69] show that the phase boundaries reduce the spall strength of composites, due to the tendentious growth of cracks at phase interfaces. As the mismatch of the phase stiffnesses is greater, the spall strength of composites becomes weaker, while the interface adhesion strength has the opposite effect on the spall strength. Hence, it is necessary to explore the spallation of nanocomposites.

When the $U_I = 0.5$ km/s, the spallation does not break out in three models, as shown in Fig. 11(a). Moreover, the peak stress for the C-SiC/Al drops below 4.0 GPa. The peak stress has no obvious change in other two models, indicating that the C-SiC/Al absorbs the impact energy efficiently for shock-wave peak stress below HEL. This suggests that the composite has better impact toughness when the shock-wave peak stress is smaller than HEL. In Fig. 11(b), for $U_I = 1.0$ km/s and peak stress is higher than HEL, a gap appears, and the profiles of stress wave separates gradually into two waves as time progresses, which marks the initiation of the cavitation (i.e. voids start to nucleate, grow and coalesce until the structure spall fracture). Furthermore, the existence of SiC/Al interface benefits the improvement of spall strength. The reason is the spall strength about 6.9 GPa for M-Al and 7.1 GPa for S-SiC/Al. However, the C-SiC/Al possessed a higher spall strength (~ 7.3 GPa) compared to the other models. The enhancement is attributed to the Orowen mechanism.

A new interference is introduced between the SiC nanoparticles and the Al-matrix at $U_{\mathrm{I}} = 1.0$ km/s. The composites are severer damaged than that of M-Al (evaluation based on void ratio), as shown in Fig. 12. The increasing in void ratio is attributed to that the peak stress of spall plate in S-SiC/Al and C-SiC/Al is about 12.2 GPa and 11.1 GPa, respectively, both exceed that of M-Al (~ 7.8 GPa). Fig. 10(b) shows the dislocation total length (DTL) evolution in the spalling after shock wave has traversed the entire model to the peak of the DTL. Because the impact of powerful rarefaction wave is far more than the recovery energy barrier of dislocations, the DTL starts to decline with same rate for three models until the cavitation occurs, which makes it bottom out (see red points in Fig. 10(b)). Before the cavitating, obviously, the DTL of M-Al is longer than that of composites, which makes M-Al more capable of absorbing impact energy. Because incident wave directly initiates the formation of high-density forest dislocations, smaller space for dislocation multiplication and slip in nanocomposites cause the dislocation pile-up in the region between nanoparticles, as shown in Fig. 13. Exceeding space capacity of dislocations is not beneficial to absorb energy since it retards the attenuation of the shock wave. In addition, shock wave stress amplification due to the unceasing wave reflection at Al/SiC interface is conduced to prepare cavitation in nanocomposites.

The dislocation strengthening is achieved via adding obstacles to retard the dislocation motion. The most contributing reinforcement mechanism is the Hall-Petch effect (fine crystal reinforcing) [70]. For the monocrystal, the dislocation strengthening is negligible, because dislocations can easily move to the crystal surface. To further confirm the existence of reinforcement by nanoparticle under shock loading, we have investigated the dynamic compression strength of the composites with bicrystals Al (B-Al) matrix. The SiC nanoparticles inside the crystal grains are modeled as shown in Fig. 14(a). All other parameters are consistent with the above model. The resulting stress-strain curve is plotted in Fig. 14(b) for $U_I = 0.5$ km/s from the force and displacement of piston. The stress-strain curve illustrates an obvious yielding. However, there are no dislocations formation in M-Al. This could be attributed to the compressive stress relaxation caused by the $U_S > U_P$. Most previous studies [71,72] have not considered a sufficient range of impact velocity and thus missed this softening effect in inconsistent with the quasi-static compression [73].

The maximum compressive stress is equal to 4.2 GPa for C-SiC/B-Al, 3.6 GPa for S-SiC/B-Al, and 3.4 GPa for B-Al, respectively, which confirms the softening effect could be suppressed by changing geometry of particles (or tuning interface) to endow the dislocation with different multiplication density and growth direction. At this point, dislocations dynamically evolve to consume part of impact energy, decreasing the elastic wave front velocity. For the cases of $U_I = 1.0$ km/s and 1.5 km/s, the elastic wave velocities are greater than that of the plastic wave.

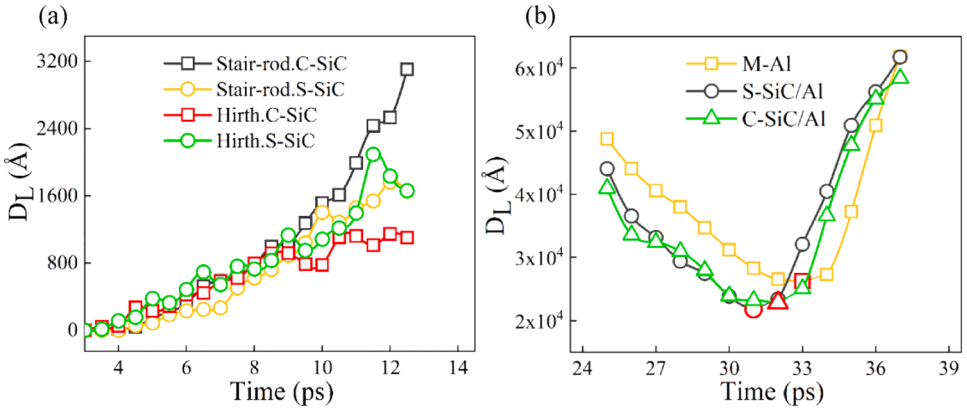


**Fig. 10.** The total length of dislocation lines as a function of simulation time: (a) for two immobile dislocations in the C-SiC/Al and S-SiC/Al at $U_I = 0.5$ km/s; (b) for all dislocations in three simulation models at $U_I = 1.0$ km/s (The points marked in red are the starting points of spall failure). (For interpretation of the references to color in this figure legend, the reader is referred to the web version of this article.)

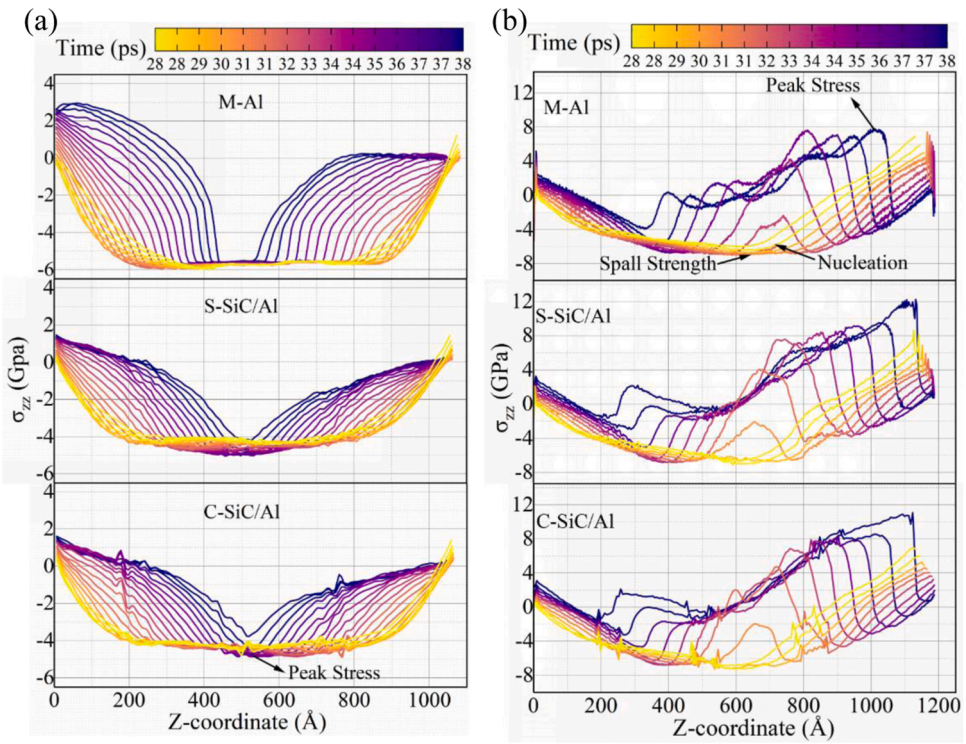


**Fig. 11.** Evolution of principal stress $\sigma_{zz}$ in the tension state at $U_I$ = (a) 0.5 km/s and (b) 1.0 km/s. The curves are colored according to the time (28–38 ps) as in the color bar. The negative values denote tensile stress, otherwise compressive stress. (For interpretation of the references to color in this figure legend, the reader is referred to the web version of this article.)

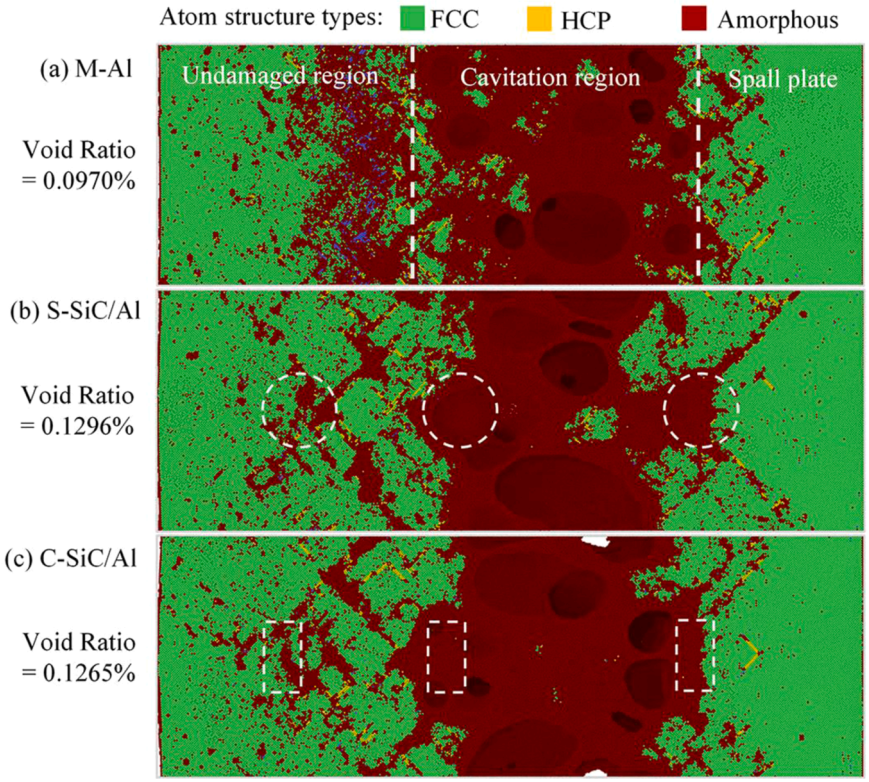


**Fig. 12.** Snapshots reveal the damage degree of samples at 38 ps and $U_I$ =1.0 km/s (a) M-Al; (b) S-SiC/Al; (c) C-SiC/Al. Dashed lines show the profile and position of reinforcements. Atoms are colored corresponding to crystal structure types: green for FCC, yellow for HCP, red for amorphous. (For interpretation of the references to color in this figure legend, the reader is referred to the web version of this article.)

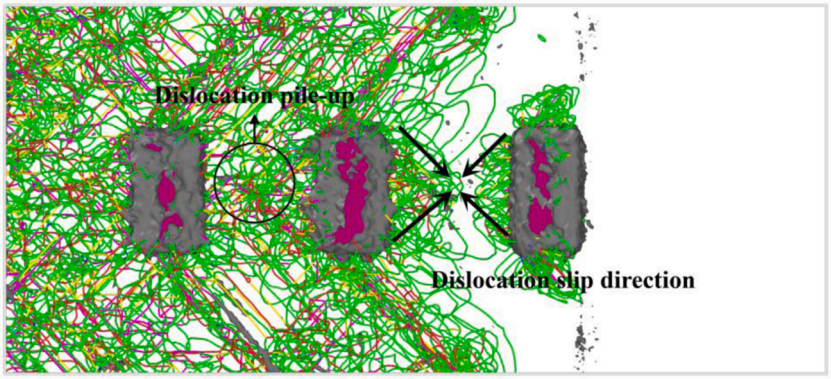


**Fig. 13.** Dislocation distribution of C-SiC/Al at $U_I = 1.0$ km/s and 10 ps. Structures of matrix are invisible for better view. The dislocation lines are colored by their type. The dark-gray surface shows the contour of C-SiC.

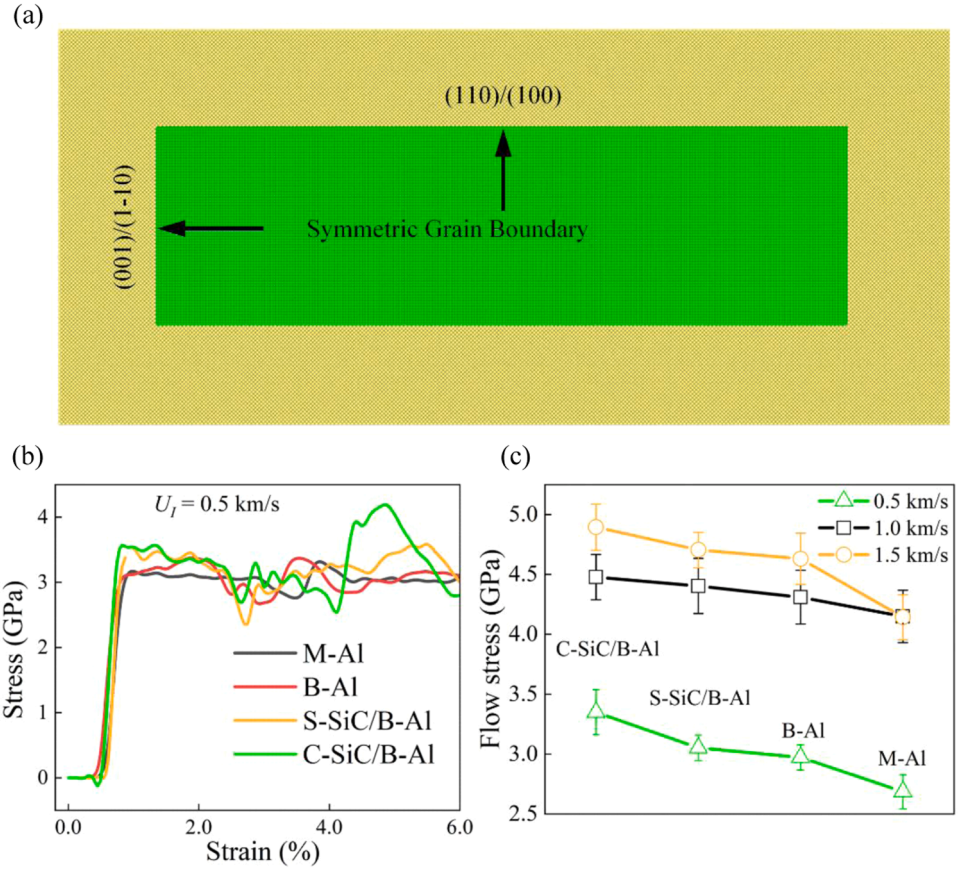


**Fig. 14.** (a) Schematics of the structure of bicrystals Al including two types of grain boundaries. The SiC particles distribution in composites remains unchanged. (b) The stress-strain curves for three models in simulation, which are calculated by force and displacement of piston. (c) Flow stress for different structures under shock loading at impact velocity of 0.5, 1.0, and 1.5 km/s. The error bars are the standard deviation.

Therefore, there is also the softening effect. Ultimately, the velocity of shock wave fronts reduces to the point where $U_S = U_p$ due to energy dissipation, whereafter materials reach dynamic compressive strength. It is worth noting that our simulation cannot reproduce this process because of the length scale limit of the MD method.

In addition, because of the existence of shock wave, the dynamic compressive strength cannot be measured by calculating principal stress in the impact direction. We directly extract the flow stress far behind shock wave front to compare the dynamic compressive strength for different structures. Fig. 14(c) shows that the qualitative dynamic strength of these structures enhances as increasing in $U_I$ except for M-Al. This is because that the lateral relaxation during shock loading is slow, resulting in pressure building up. As a result, the dislocations are more difficult to slip. In contrast, there are no strong dislocation obstacles in M-Al, which leads to relatively inconspicuous dislocation-controlled shock-strengthening. The dynamic strength increases substantially when $U_I$ changes from 0.5 km/s to 1.0 k/m, because of the formation of high-density forest dislocation. Some atomic configuration changes (such as dislocation tangles and pile-up) can retain after shock wave front through, governing the strength of subsequent dynamic compression or recovering of shocked materials. The maximum flow stress occurs in C-SiC/B-Al, evidencing that the strongest obstruction for

dislocation slip is induced by C-SiC nanoparticles.

## 4. Conclusions

We have investigated the shock responses of ceramic-metal nanocomposites to contrast with pure metal one using molecular dynamics simulations. We have examined three typical impact velocities $U_I = 0.5$, 1.0, 1.5 km/s and three model systems including S-SiC/Al nanocomposite, C-SiC/Al nanocomposite, and pure Al. Our simulations reveal that when peak stress at $U_I = 0.5$ km/s falls below the HEL of M-Al, only elastic shock wave forms. On the contrary, the plastic deformation occurs in the nanocomposites. The reason is that the reflected shear stress wave surpasses the critical value. The interaction between elastic wave and different interface governs dislocation structures evolution.

Under $U_I = 1.0$ km/s that brings about peak stress above HEL, the shock wave is separated into elastic and plastic waves. The striking discovery is that the effect of nanoparticles on dislocation structure has changed from multiplying to retarding dislocations when the impact velocity exceeds the Hugoniot elastic limit. The cause is that formed dislocations exceed space capacity. Dislocations pile-up at interface improves spall strength of composites. However, unceasing reflection and amplification of shock waves at interface exacerbate the shock damage.

Shock-induced softening effect originates from the distinction in atomic velocity in different shock regions, which is suppressed by increasing the dissipation of impact energy. Dynamic compressive strength of the structures (except for M-Al) increases with the impact velocity, possessing the highest strength in C-SiC/B-Al. The results indicate that the optimum nanoparticle geometry is to make dislocation multiplying and tangling as much as possible to achieve a higher impact energy dissipation and flow stress. Our atomistic insights might benefit in understanding the mechanism of laser shock processing. Our results might be helpful in applying LSP on composites and designing advanced ceramic-metal composite for high shock-tolerant protective materials.

## CRediT authorship contribution statement

**Kuixin Lin:** Conceptualization, Investigation, Experiment, Formal analysis, Writing-original draft. **Meng Zeng:** Investigation. **Hongmei Chen:** Supervision, Funding acquisition. **Xiaoma Tao:** Supervision, Writing - review & editing, Funding acquisition. **Qing Peng:** Supervision, Writing-review & editing. **Yong Du:** Supervision, Writing-review & editing. **Yifang Ouyang:** Supervision, Writing-review & editing, Funding acquisition.

## Declaration of Competing Interest

The authors claim that there is no conflict interest between the authors and their institutes.

## Data availability

No data was used for the research described in the article.

## Acknowledgments

The authors gratefully acknowledge the financial support from the National Natural Science Foundation of China (Grant No. 11964003) and the Guangxi Natural Science Foundation (Grant No. 2019GXNSFAA185058, 2018GXNSFAA281291). Q. P. would like to acknowledge the support provided by LiYing Program of the Institute of Mechanics, Chinese Academy of Sciences (No. E1Z1011001). The authors are grateful to Prof. Fei Gao for his proofreading and valuable suggestions. All calculations were performed in Multi-function Computer Center of Guangxi University.

## References

[1] Casati R, Vedani M. Metal matrix composites reinforced by nano-particles—a review. Metals (Basel) 2014;4:65–83.
[2] Ibrahim IA, Mohamed FA, Lavernia EJ. Particulate reinforced metal matrix composites—a review. J Mater Sci 1991;26:1137–56.
[3] Hu Y, Cong W. A review on laser deposition-additive manufacturing of ceramics and ceramic reinforced metal matrix composites. Ceram Int 2018;44:20599–612.
[4] Riquelme A, Escalera-Rodríguez M, Rodrigo P, Otero E, Rams J. Effect of alloy elements added on microstructure and hardening of Al/SiC laser clad coatings. J Alloy Compd 2017;727:671–82.
[5] Chawla N, Shen YL. Mechanical behavior of particle reinforced metal matrix composites. Adv Eng Mater 2001;3:357–70.
[6] Sahin Y, Acılar M. Production and properties of SiCp-reinforced aluminium alloy composites. Compos Part A Appl Sci 2003;34:709–18.
[7] Shabani MO, Mazahery A. The synthesis of the particulates Al matrix composites by the compocasting method. Ceram Int 2013;39:1351–8.
[8] El-Kady O, Fathy A. Effect of SiC particle size on the physical and mechanical properties of extruded Al matrix nanocomposites. Mater Des 2014;54:348–53.
[9] Guo X, Guo Q, Li Z, Fan G, Xiong D, Su Y, Zhang J, Gan C, Zhang D. Interfacial strength and deformation mechanism of SiC–Al composite micro-pillars. Scr Mater 2016;114:56–9.
[10] Ulianitsky V, Shtertser A, Batraev I, Rybin D. Fabrication of layered ceramic-metal composites by detonation spraying. Ceram Int 2020;46:27903–8.
[11] El-Hofy M, El-Hofy H. Laser beam machining of carbon fiber reinforced composites: a review. Int J Adv Manuf Technol 2018;101:2965–75.
[12] Zhang J, Perez RJ, Lavernia EJ. Dislocation-induced damping in metal matrix composites. J Mater Sci 1993;28:835–46.
[13] Ye T, Xu Y, Ren J. Effects of SiC particle size on mechanical properties of SiC particle reinforced aluminum metal matrix composite. Mater Sci Eng A Struct 2019;753:146–55.
[14] Akbarpour MR, Salahi E, Hesari FA, Kim HS, Simchi A. Effect of nanoparticle content on the microstructural and mechanical properties of nano-SiC dispersed bulk ultrafine-grained Cu matrix composites. Mater Des 2013;52:881–7.
[15] Queyreau S, Ghiath M, Benoit D. Orowan strengthening and forest hardening superposition examined by dislocation dynamics simulations. Acta Mater 2010;58:5586–95.
[16] Li CL, Mei QS, Li JY, Chen F, Ma Y, Mei XM. Hall-Petch relations and strengthening of Al-ZnO composites in view of grain size relative to interparticle spacing. Scr Mater 2018;153:27–30.
[17] Zhang Z, Chen DL. Consideration of Orowan strengthening effect in particulate-reinforced metal matrix nanocomposites: a model for predicting their yield strength. Scr Mater 2006;54:1321–6.
[18] Li J, Liu B, Fang Q, Huang Z, Liu Y. Atomic-scale strengthening mechanism of dislocation-obstacle interaction in silicon carbide particle-reinforced copper matrix nanocomposites. Ceram Int 2017;43:3839–46.
[19] Kumar M, Begum S, Pruncu CI, Shahedi Asl M. Role of homogeneous distribution of SiC reinforcement on the characteristics of stir casted Al–SiC composites. J Alloy Compd 2021;869:159250.
[20] Jamali G, Nourouzi S, Jamaati R. Manufacturing of gradient Al/SiC composite wire by friction stir back extrusion. CIRP J Manuf Sci Technol 2021;35:735–43.
[21] Molian P, Molian R, Nair R. Laser shock wave consolidation of nanodiamond powders on aluminum 319. Appl Surf Sci 2009;255:3859–67.
[22] Zhang X, Lu S, Zhang B, Tian X, Kan Q, Kang G. Dislocation–grain boundary interaction-based discrete dislocation dynamics modeling and its application to bicrystals with different misorientations. Acta Mater 2021;202:88–98.
[23] Bringa EM, Caro A, Wang Y, Victoria M, McNaney JM, Remington BA, Swygenhoven VH. Ultrahigh strength in nanocrystalline materials under shock loading. Science 2005;309:1838–41.
[24] Xiang M, Liao Y, Wang K, Lu G, Chen J. Shock-induced plasticity in semi-coherent {111} Cu-Ni multilayers. Int J Plast 2018;103:23–38.
[25] Zhang L, Huang Y, Shu H, Chen B, Chen X, Ma Y, Liu W. Spallation damage of 90W–Ni–Fe alloy under laser-induced plasma shock wave. J Mater Res Technol 2022;17:1731–9.
[26] Ecault R, Boustie M, Touchard F, Pons F, Berthe L, Chocinski-Arnault L, et al. A study of composite material damage induced by laser shock waves. Compos Part A Appl Sci 2013;53:54–64.
[27] Zhan JM, Yao XH, Zhang XQ. Shock response of metal-ceramic nanolayered Composites. Compos Part B Eng 2020;199:108272.
[28] Ramnath BV, Elanchezhian C, Jaivignesh M, Rajesh S, Parswajinan C, Ghias ASA. Evaluation of mechanical properties of aluminium alloy–alumina–boron carbide metal matrix composites. Mater Des 2014;58:332–8.
[29] Ozden S, Ekici R, Nair F. Investigation of impact behaviour of aluminium based SiC particle reinforced metal–matrix composites. Compos Part A Appl Sci 2007;38(2):484–94.
[30] Cerit AA. Investigation of the low-speed impact behavior of dual particle size metal matrix composites. Mater Des 2014;57:330–5.
[31] Tavakol M, Mahnama M, Naghdabadi R. Shock wave sintering of Al/SiC metal matrix nano-composites: a molecular dynamics study. Comput Mater Sci 2016;125:255–62.
[32] Li R, Wang Y, Xu N, Yan Z, Li S, Zhang M, Almer J, Ren Y, Wang Y. Unveiling the origins of work-hardening enhancement and mechanical instability in laser shock peened titanium. Acta Mater 2022;229:117810.

[33] Zhao J, Pan X, Li J, Huang Z, Kan Q, Kang G, Zhou L, Zhang X. Laser shock peened Ti-6Al-4V alloy: experiments and modeling. Int J Mech Sci 2022;213:106874.
[34] Wen Y, Wu Y, Hua L, Xie L, Wang L, Zhang L-C, et al. Effects of shot peening on microstructure evolution and mechanical properties of surface nanocrystal layer on titanium matrix composite. Mater Des 2021;206:109760.
[35] Wang C, Wang L, Wang C, Li K, Wang X. Dislocation density-based study of grain refinement induced by laser shock peening. Opt Laser Technol 2020;121:105827.
[36] Lv J, Luo K, Lu H, Wang Z, Liu J, Lu J. Achieving high strength and ductility in selective laser melting Ti-6Al-4V alloy by laser shock peening. J Alloy Compd 2022;899:163335.
[37] Ji F, Deng W, Lu H, Wu L, Luo K, Lu J. Laser shock peening-induced misfit dislocation at interfaces between HCP and BCC crystals of Ti6Al4V alloy and the corresponding dislocation patterns in two phases. Surf Coat Technol 2022;440:128513.
[38] Cui C, Cui X, Li X, Luo K, Lu J, Ren X, Zhou J, Fang C, Farkouh R, Lu Y. Plastic-deformation-driven SiC nanoparticle implantation in an Al surface by laser shock wave: mechanical properties, microstructure characteristics, and synergistic strengthening mechanisms. Int J Plast 2018;102:83–100.
[39] Sun R, Cao Z, Che Z, Zhang H, Zou S, Wu J, Guo W. A combined experimental-numerical study of residual stress and its relaxation on laser shock peened SiC particle-reinforced 2009 aluminum metal matrix composites. Surf Coat Technol 2022;430:127988.
[40] Wen Y, Wu Y, Hua L, Xie L, Wang L, Zhang L, et al. Effects of shot peening on microstructure evolution and mechanical properties of surface nanocrystal layer on titanium matrix composite. Mater Des 2021;206:109760.
[41] Lin D, Motlag M, Saei M, Jin S, Rahimi RM, Bahr D, Cheng GJ. Shock engineering the additive manufactured graphene-metal nanocomposite with high density nanotwins and dislocations for ultra-stable mechanical properties. Acta Mater 2018;150:360–72.
[42] Zhang C, Godbole A, Michal G, Lu C. High shock resistance and self-healing ability of graphene/nanotwinned Cu nanolayered composites. J Alloy Compd 2021;860:158435.
[43] Liu X, Wang F, Wu H, Wang W. Strengthening metal nanolaminates under shock compression through dual effect of strong and weak graphene interface. Appl Phys Lett 2014;104:231901.
[44] Lin D, Saei M, Suslov S, Jin S, Cheng GJ. Super-strengthening and stabilizing with carbon nanotube harnessed high density nanotwins in metals by shock loading. Sci Rep 2015;5:1–11.
[45] Jiang M, Devincre B, Monnet G. Effects of the grain size and shape on the flow stress: a dislocation dynamics study. Int J Plast 2019;113:111–24.
[46] Qin S, Chen C, Zhang G, Wang W, Wang Z. The effect of particle shape on ductility of SiCp reinforced 6061 Al matrix composites. Mater Sci Eng A Struct 1999;272:363–70.
[47] Plimpton S. Fast parallel algorithms for short-range molecular dynamics. J Comput Phys 1995;117:1–19.
[48] Winey JM, Kubota A, Gupta YM. A thermodynamic approach to determine accurate potentials for molecular dynamics simulations: thermoelastic response of aluminum. Modell Simul Mater Sci Eng 2009;17:055004.
[49] Zepeda-Ruiz LA, Stukowski A, Oppelstrup T, Bertin N, Barton NR, Freitas R, Bulatov VV. Atomistic insights into metal hardening. Nat Mater 2021;20:315–20.
[50] Zimmerman JA, Winey JM, Gupta YM. Elastic anisotropy of shocked aluminum single crystals: use of molecular dynamics simulations. Phys Rev B 2011;83:184113.
[51] Erhart P, Albe K. Analytical potential for atomistic simulations of silicon, carbon, and silicon carbide. Phys Rev B 2005;71:035211.
[52] Xie L, Sun T, He C, Deng J, Yi H, Yang X, Qin Q, Peng Q. Enhancement of toughness of SiC through compositing SiC–Al interpenetrating phase composites. Nanotechnology 2020;31:135706.
[53] Dandekar CR, Shin YC. Molecular dynamics based cohesive zone law for describing Al–SiC interface mechanics. Compos Part A Appl Sci 2011;42:355–63.
[54] DeVries M, Subhash G, Awasthi A. Shocked ceramics melt: an atomistic analysis of thermodynamic behavior of boron carbide. Phys Rev B 2020;101:144107.
[55] Stukowski A. Visualization and analysis of atomistic simulation data with OVITO-the open visualization tool. Model Simul Mater Sci Eng 2010;18:15012.
[56] Stukowski A. Structure identification methods for atomistic simulations of crystalline materials. Model Simul Mater Sci Eng 2012;20:045021.
[57] Stukowski A, Bulatov VV, Arsenlis A. Automated identification and indexing of dislocations in crystal interfaces. Model Simul Mater Sci Eng 2012;20:85007.
[58] He L, Wang F, Zeng X, Yang X, Qi Z. Atomic insights into shock-induced spallation of single-crystal aluminum through molecular dynamics modeling. Mech Mater 2020;143:103343.
[59] Liu ZL, Sun JS, Li R, Zhang XL, Cai LC. Comparative study on two melting simulation methods: melting curve of gold. Commun Theor Phys 2016;65:613.
[60] Pu C, Yang X, Xiao D, Cheng J. Molecular dynamics simulations of shock melting in single crystal Al and Cu along the principle Hugoniot. Mater Today Commun 2021;26:101990.
[61] Davison L, Graham R. Shock compression of solids. Phys Rep 1979;55:255–379.
[62] Peng Q, Meng F, Yang Y, Lu C, Deng H, Wang L, De S, Gao F. Shockwave generates <100>dislocation loops in bcc iron. Nat Commun 2018;9:1–6.
[63] Norman GE, Yanilkin AV. Homogeneous nucleation of dislocations. Phys Solid State 2011;53:1614–9.
[64] Hussein AM, Rao SI, Uchic MD, Dimiduk DM, ElAwady JA. Microstructurally based cross-slip mechanisms and their effects on dislocation microstructure evolution in fcc crystals. Acta Mater 2015;85:180–90.
[65] Ritchie RO. The conflicts between strength and toughness. Nat Mater 2011;10:817–22.
[66] Lebar A, Aguiar R, Oddy A, Petel OE. Particle surface effects on the spall strength of particle-reinforced polymer matrix composites. Int J Impact Eng 2021;150:103801.
[67] Chen J, Tschopp M, Dongare A. Role of nanoscale Cu/Ta interfaces on the shock compression and spall failure of nanocrystalline Cu/Ta systems at the atomic scales. J Mater Sci 2017;53:5745–65.
[68] Lin K, Li D, Song S, Ye Z, Jiang W, Qin QH. Enhanced mechanical properties of 4H-SiC by epitaxial carbon films obtained from bilayer graphene. Nanotechnology 2020;31:195702.
[69] Fensin SJ, Walker EK, Cerreta EK, Trujillo CP, Martinez DT, Gray III GT. Dynamic failure in two-phase materials. J Appl Phys 2015;118:235305.
[70] Sanaty-Zadeh A. Comparison between current models for the strength of particulate-reinforced metal matrix nanocomposites with emphasis on consideration of Hall–Petch effect. Mater Sci Eng A Struct 2012;531:112–8.
[71] Liu J, Liu G, Ye C, Chen K, Hu J, Yu Y, Shen Y. Multiscale investigation of shear relaxation in shock loading: a top-down perspective. Mater Des 2022;220:110839.
[72] Luo SN, Han LB, Xie Y, An Q, Zheng L, Xia K. The relation between shock-state particle velocity and free surface velocity: a molecular dynamics study on single crystal Cu and Silica Glass. J Appl Phys 2008;103:093530.
[73] Gnjidić Ž, Božić D, Mitkov M. The influence of SiC particles on the compressive properties of metal matrix composites. Mater Charact 2001;47(2):129–38.